Mid-infrared broadband circular polarizer based on Weyl semimetals

CHIYU YANG,[1] **BO ZHAO,**[2] **WENSHAN CAI,**[3] **AND ZHUOMIN M. ZHANG**[1,*]

[1]*George W. Woodruff School of Mechanical Engineering, Georgia Institute of Technology, Atlanta, GA 30332, USA*

[2]*Department of Mechanical Engineering, University of Houston, Houston, TX 77204, USA*

[3]*School of Electrical and Computer Engineering, Georgia Institute of Technology, Atlanta, GA 30332, USA*

[*]*zhuomin.zhang@me.gatech.edu*

Abstract: As a three-dimensional topological phase of matter, Weyl semimetals possess extremely large gyrotropic optical response in the mid-infrared region, leading to the strong chiral anomaly. This study proposes a circular polarizer design with a double-WSM-layer structure. It is theoretically shown that the proposed polarizer possesses a high circular polarization efficiency and high average transmittance in the wavelength region from 9 μm to 15 μm at incidence angles up to 50°. The modified 4×4 matrix method is used to calculate the circularly polarized transmittance of Weyl semimetals in thin-film or multilayer structures. The temperature dependence on the transmittance is also examined to demonstrate the flexibility of the proposed polarizer in a varying temperature environment. This study reveals the technological prospect that Weyl semimetals are promising candidates for high-performance circular polarizers in infrared spectroscopy and polarimetry.

1. Introduction

Circularly polarized (CP) optical radiation is characterized by left-handed circularly polarized (LCP) or right-handed circularly polarized (RCP) state. Depending on the polarization, CP radiation interacts differently with chiral materials, leading to unique phenomena such as magneto-optical effect [1], circular dichroism [2–4], and spin-hall effect of light [5]. While optical devices in the visible or near-infrared regions have been widely investigated, very few studies dealt with CP radiation at longer wavelengths due to the fact that most optical materials become opaque in the mid-infrared spectral region [6,7]. The control and manipulation of CP radiation at longer wavelengths have vital importance in remote sensing, landmine detection, biomedical diagnostics, and surface and materials characterization [8,9].

Traditionally, CP optical radiation is typically obtained from unpolarized radiation by combining a linear polarizer and a quarter-wave plate. Besides the inherent narrowband nature, their bulky sizes prevent them from being integrated into a compact optical system [10]. Metamaterials with periodical structures may enable polarization control with subwavelength thicknesses [11]. Various circular polarizers made of three-dimensional (3D) chiral metamaterial [12,13], two-dimensional (2D) chiral metasurface [14,15], and metasurface with multilayer structures [16], are proposed to achieve both highly selective transmittance and compactness. However, due to the nature of plasmonic metamaterial, these polarizers suffer from either a relatively low circular polarization efficiency or a narrow spectral bandwidth with high efficiency.

A Weyl semimetal (WSM) is a topological phase of matter whose band structure contains pairs of Weyl nodes, which are considered as magnetic monopoles and antimonopoles in the momentum space [17–19]. The Weyl nodes act as a source or drain of Berry curvature with positive or negative chiral charges and the corresponding Chern numbers [20,21]. Achieving such WSMs requires breaking either the time-reversal or inversion symmetry, or both [22].

Symmetry-breaking WSMs have been experimentally observed since 2015 [23,24]. However, only until recently, time-reversal-breaking WSMs have been discovered [25,26]. The family of time-reversal-breaking semimetals have giant magneto-optical effect in the broad infrared region without requiring an external magnetic field. Examples of magnetic WSMs are pyrochlore iridates (e.g., Eu_2IrO_7) [27], ferromagnetic spinels (e.g., $HgCr_2Se_4$) [28], Heusler ferromagnets (e.g., Co_2MnAl) [29], and Co-based shandites (e.g., $Co_3S_2Se_3$) [30]. These materials have lately attracted significant interest due to their potential applications in the design of optical isolators [31], thermal emitters that disobey Kirchhoff's law [32,33], and chiral terahertz emitters [34].

This paper describes a mid-infrared circular polarizer based on thin films of magnetic WSMs. Researchers have recently reported the spin-resolved properties of WSMs such as circular emission and circular dichroism [35,36]. However, the analysis of thin-film and multilayer WSMs based on rigorous electromagnetic wave formulation has not been reported. Here, a modified 4×4 matrix method that fully considers the effects of multiple reflections and interference is employed to analyze the transmission characteristics of WSM films. The effects of thickness and the number of layers on the circularly polarized transmittance are investigated. It is found that the transmission of the double-WSM-layer structure is highly selectively for circularly polarized optical radiation in the mid-infrared region and can serve as a circular polarizer with a high degree of polarization. The influences of incidence angle and temperature on the performance of the circular polarizer are also examined.

2. Methodology

The band structure of WSM contains an even number of nondegenerate band touching points (Weyl nodes) that shrunken from the Fermi surface. This study considers the simplest case where the WSM hosts two Weyl nodes with opposite chirality separated by a wave vector $2\mathbf{b}$ in the momentum space. This kind of WSM has been experimentally demonstrated recently [37]. The nontrivial topology of WSMs has exotic electromagnetic responses that are described by the axion electrodynamics. The displacement field $\mathbf{D}$ and the electric field $\mathbf{E}$ in the frequency domain obey the modified constitutive relation [31,32,38]:

$$\mathbf{D} = \varepsilon_0\varepsilon_d\mathbf{E} + i\frac{e^2}{2\pi^2\hbar\omega}\mathbf{b} \times \mathbf{E} \tag{1}$$

where ε_0 is the permittivity of vacuum, ε_d is the dielectric function (relative permittivity) of the corresponding Dirac semimetal with $\mathbf{b} = 0$, $i = \sqrt{-1}$, e is the electron charge, $\hbar$ is the reduced Planck constant, and ω is the angular frequency. A brief derivation is provided in Appendix A. The inset in Fig. 1(a) shows the electronic band structure of the type I magnetic WSM near the Weyl nodes with the same energy but separated by 2b along the k_z direction. In this case, the dielectric function tensor defined based on $\mathbf{D} = \varepsilon_0\bar{\bar{\varepsilon}}\mathbf{E}$ for the WSM is written as [32]

$$\bar{\bar{\varepsilon}} = \begin{bmatrix} \varepsilon_d & i\varepsilon_a & 0 \\ -i\varepsilon_a & \varepsilon_d & 0 \\ 0 & 0 & \varepsilon_d \end{bmatrix} \tag{2}$$

where the off-diagonal terms are purely imaginary with opposite signs, and ε_a is given by

$$\varepsilon_a = \frac{be^2}{2\pi^2\hbar\omega\varepsilon_0} \tag{3}$$

The existence of the off-diagonal asymmetric terms in the dielectric function breaks the Lorentz reciprocity [39], and therefore, the conventional Kirchhoff's law may be violated [40]. Such

nonreciprocity is related to the anomalous Hall effect and chiral magnetic effect [41]. The diagonal terms are the same and can be obtained by the two-band model using the Kubo-Greenwood formalism [32,38,41,42]:

$$\varepsilon_d = \varepsilon_b + i\frac{\sigma}{\omega\varepsilon_0} \tag{4}$$

where ε_b is the background dielectric function and σ is the bulk conductivity given by [31,32]

$$\sigma = \frac{\varepsilon_0 r_s g E_F}{6\hbar}\Omega G(E_F\Omega/2)$$
$$+ i\frac{\varepsilon_0 r_s g E_F}{6\pi\hbar}\left\{\frac{4}{\Omega}\left[1 + \frac{\pi^2}{3}\left(\frac{k_B T}{E_F}\right)^2\right] + 8\Omega\int_0^{\xi_c}\frac{G(\xi E_F) - G(E_F\Omega/2)}{\Omega^2 - 4\xi^2}\xi d\xi\right\} \tag{5}$$

In Eq. (5), $r_s = e^2/(4\pi\varepsilon_0\hbar v_F)$ is the effective fine structure constant defined based on the Fermi velocity v_F; g is the number of Weyl nodes; E_F is the Fermi energy; $\Omega = \hbar(\omega + i\tau^{-1})/E_F$ is the complex frequency normalized by $E_F/\hbar$, where τ^{-1} is the scattering rate as in the Drude model; $G(E) = n(-E) - n(E)$, where $n(E) = \{\exp[(E - E_F)/k_B T] + 1\}^{-1}$ is the Fermi-Dirac distribution function with k_B being the Boltzmann constant; and $\xi_c = E_c/E_F$ is the normalized cutoff energy, beyond which the band dispersion is no longer linear [42].

The parameters used in the present work are taken from Zhao et al. [32] such that $\varepsilon_b = 6.2$, $\xi_c = 3$, $\tau = 1000$ fs, $g = 2$, $b = 2 \times 10^9$ m^{-1}, and $v_F = 8.3 \times 10^4$ m/s. The relative permeability μ is taken to be 1; this assumption has been used in dealing with magneto-optical effects [43]. The Fermi energy (or Fermi level) is a function of temperature. In the present study, the temperature dependence of E_F is calculated according to the formula given by Ashby and Carbotte [44], giving $E_F = 0.15$ eV at room temperature that is used as the default. The calculated room-temperature dielectric functions ε_a and ε_d are plotted in Fig. 1(a) in the wavelength (λ) region from 2 μm to 20 μm. The gyrotropic effect is often characterized by the ratio $\gamma = |\varepsilon_a|/|\varepsilon_d|$, which is on the order of one for WSMs in the mid-infrared region. For a traditional magneto-optical material with a moderate magnetic field $B \approx 1$ T, γ is on the order of 0.01. A magnetic field over 100 T is required for traditional magneto-optical materials in order for γ to be around 1. This is the reason why a mid-infrared circular polarizer was not found in traditional magneto-optical materials.

The schematic of the proposed circular polarizer is shown in Fig. 1(b). It consists of two WSM films separated by a distance d in a vacuum with a submicron film thickness t. Ultrathin WSMs with thicknesses as small as 50 nm have recently been experimentally realized [45,46]. The WSM films are arranged such that the separation vector **b** of the Weyl nodes is parallel to the z-axis. This arrangement is referred to as the Faraday geometry because the propagating direction at normal incidence is in parallel with the vector **b**, which is analogous to an applied magnetic field [47].

The 4×4 transfer matrix method, originally put forward by Teitler and Henvis [48], has been widely used in calculating the optical properties of the anisotropic materials and thin films [49–51]. Because the TE or TM waves are defined based on the plane of incidence, the applied boundary conditions need to be projected onto the coordinate axes for an arbitrary incidence (i.e., when the plane of incidence is not parallel or perpendicular to the coordinate axes). This makes the formulation relatively complex and laborious in the algorithm, though some modifications have been developed over time. Recently, Wu et al. [52] developed a modified 4×4 transfer matrix method that uses a rotational transformation technique to circumvent the projection operation. By relating the electromagnetic fields and their derivatives for the incident and transmitted radiation, one can obtain the 4×4 transfer coefficient matrix from which the Fresnel transmission coefficients t_{jk} can be calculated with linear polarization indices (*pp ps sp ss*) or circular polarization indices (−− −+ +− ++). Here, the first and second indices specify the polarization for the incident and transmitted waves. For linear polarization, $j,k = [p,s]$ where p and s denote the p-polarized (transverse magnetic, TM) and s-polarized (transverse electric,

(a)

(b)
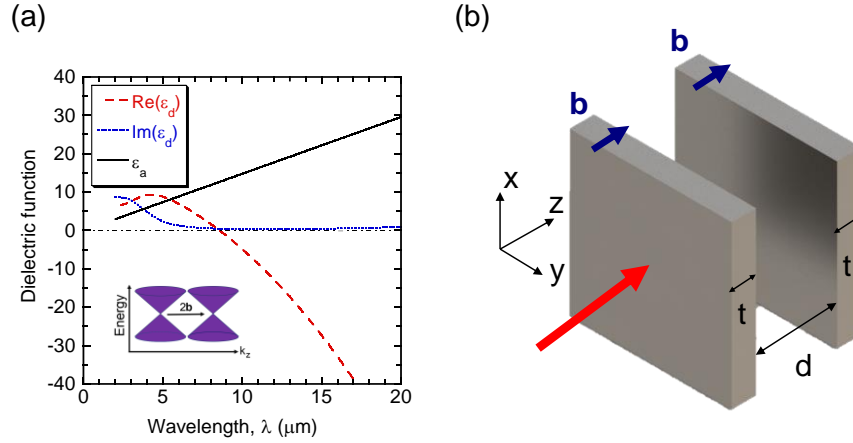
Fig. 1. Illustration of the Weyl semimetal and proposed polarizer structure. (a) Dielectric functions of the WSM. The inset at the lower-left corner is a schematic of the electronic band structure of the WSM with two Weyl nodes, separated by 2b along the k_z direction; (b) schematic of the proposed double-WSM-layer circular polarizer with thin WSM films (thickness t) separated by a vacuum spacing d.

TE) waves. For circularly polarized radiation, $j,k = [-,+]$ and the indices $-$ and $+$ signify LCP and RCP, respectively. The Fresnel coefficients are defined based on the ratio of the electric fields with the specified polarization for both co-polarization and cross-polarization cases. The detailed formulation can be found from Ref. [52] and will not be repeated here.

The relationships between the electric fields for circularly and linearly polarized waves are given by $E_- = (E_p - iE_s)/\sqrt{2}$ for LCP radiation and $E_+ = (E_p + iE_s)/\sqrt{2}$ for RCP radiation [53]. The conversion of the Fresnel transmission coefficients between linear and circular polarization can be expressed in the matrix form as

$$\begin{bmatrix} t_{--} & t_{+-} \\ t_{-+} & t_{++} \end{bmatrix} = \begin{bmatrix} 1 & -i \\ 1 & i \end{bmatrix} \begin{bmatrix} t_{pp} & t_{sp} \\ t_{ps} & t_{ss} \end{bmatrix} \begin{bmatrix} 1 & -i \\ 1 & i \end{bmatrix}^{-1} \tag{6}$$

which is a compact form for the same equations given in Refs. [53,54]. Since the media on both sides of the polarizer are vacuum, t_{jk} has the same expression whether it is defined by the ratio of the electric fields or magnetic fields. The energy transmittance components are the absolute square of Fresnel's coefficients $T_{jk} = |t_{jk}|^2$ [7]. The overall transmittance for a specific polarization is given by the summation of the co-polarization and cross-polarization components, i.e., $T_- = T_{--} + T_{-+}$ and $T_+ = T_{+-} + T_{++}$ for circular polarization and $T_p = T_{pp} + T_{ps}$ and $T_s = T_{ss} + T_{sp}$ for linear polarization. One can replace T and t by R and r in the above equations to describe the reflectance and Fresnel's reflection coefficients. Similar to the definition for linear polarizers, the circular polarization efficiency can be defined as [9,55]

$$\eta_{cp} = \frac{T_+ - T_-}{T_+ + T_-} \tag{7}$$

It describes the degree of circular polarization of the transmitted optical radiation. The value of η_{cp} lies between -1 (completely LCP) and $+1$ (completely RCP). The average transmittance is given by the mean value for the LCP and RCP transmission such that $T_{avg} = (T_- + T_+)/2$.

3. Results

The effects of thickness and number of layers of WSMs are investigated and the results are shown in Fig. 2 at normal incidence ($\theta_i = 0°$). Since the structure has rotational symmetry about the *z*-axis, the plots stand for all azimuthal angles. The transmittance and circular polarization efficiency for single- or double- WSM-layer structures are compared. The refractive indices for LCP and RCP in a WSM layer are given by $n_- = \sqrt{\varepsilon_d + \varepsilon_a}$ and $n_+ = \sqrt{\varepsilon_d - \varepsilon_a}$ according to [47]. Due to the high gyrotropic optical response of WSMs, n_- and n_+ have a large difference, giving rise to the clear distinction between the LCP and RCP transmission. The transmittance of LCP and RCP optical radiation of a single WSM layer with film thickness $t = 0.3$ μm is shown in Fig. 2(a) for 2 μm $< \lambda <$ 20 μm. Around $\lambda = 6$ μm, the transmittance for LCP is greater than that for RCP. Beyond $\lambda \approx 8$ μm, the transmittance of RCP exceeds that of LCP and reaches a peak near 14 μm. Clearly, the WSM film has a better polarization selectivity in the longer wavelength region. The circular polarization efficiency η_{cp} and the average transmittance T_{avg} are plotted in Fig. 2(b) for 8 μm $< \lambda <$ 20 μm. The highest T_{avg} occurs at $\lambda \approx 13$ μm with the value near 0.5; however, the maximum η_{cp} is only about 0.85. Figures 2(c) and 2(d) present the result of a WSM layer of $t = 0.6$ μm. Increasing the thickness causes an increase in the absorption for both LCP and RCP optical radiation and a reduction of the transmittance. Nevertheless, T_- declines faster than T_+ as the thickness increases, leading to a higher circular polarization efficiency as shown in Fig. 2(d). In other words, simply increasing the WSM thickness can achieve higher circular polarization efficiency at the cost of diminishing the average transmittance. The trade-off can be prevented by using the multilayer structure that consists of two WSM layers separated by a vacuum, as shown in Figs. 2(e) and 2(f) for the proposed double-WSM-layer polarizer. A vacuum gap between the two WSM films introduces an extra pair of boundaries that can strengthen the polarization selectivity. The value of η_{cp} is greater than 0.97 for 8 μm $< \lambda <$ 20 μm and exceeds 0.99 about the peak region near 14 μm, manifests that the multilayer structure is preferred to achieve higher circular polarization efficiency with larger average transmittance in the wavelength region from 8 μm to 20 μm. A spacer could be used to create the gap. Another way is to use a suitable substrate that is transparent in this wavelength region with a refractive index close to 1.

Due to wave interference effects, the transmittance spectrum for RCP exhibits two peaks for single- and double-WSM-layer structures, as shown in Figs. 2(c) and 2(e), respectively. By placing two films apart, the peaks couple with each other and form a broad high-transmission region from 8 μm to 17 μm. The multilayer structure also effectively suppresses the transmission for LCP at longer wavelengths, giving a higher circular polarization efficiency from 8 μm to 20 μm as shown in Fig. 2(f). Changing the gap distance *d* between the two WSM thin films modifies the position of the peaks of RCP transmittance. To accomplish both high circular polarization efficiency and high average transmittance, the distance can be finely tuned to find the optimal transmittance spectrum. Single WSM layer without such tunability cannot achieve both high circular polarization efficiency and high average transmittance. Multilayers with three or more WSM films have also been examined but the results did not show any significant improvement on the performance but the design complexity of the polarizer and are not presented here. Notice that if the direction of **b** is reversed, T_- and T_+ will swap, so that the polarizer will become LCP transmitted while RCP radiation will be mostly reflected or absorbed. This can be done either by flip the polarizer or change the direction of **b**.

To gain a better understanding of the polarizer, the spectral transmittance and reflectance components of the double-WSM-layer structure are calculated for both linear and circular polarizations, as shown in Fig. 3. The transmittance components for circular polarization are shown in Fig. 3(a). The cross-polarization components are zero ($T_{-+} = T_{+-} = 0$) at normal incidence and are not shown. Figure 3(b) plots the reflectance components for circular polarization. Here, the co-polarization components are zero ($R_{--} = R_{++} = 0$) and the reflectance is from cross-polarization due to the handedness reversal upon reflection. In the long wavelength region, the
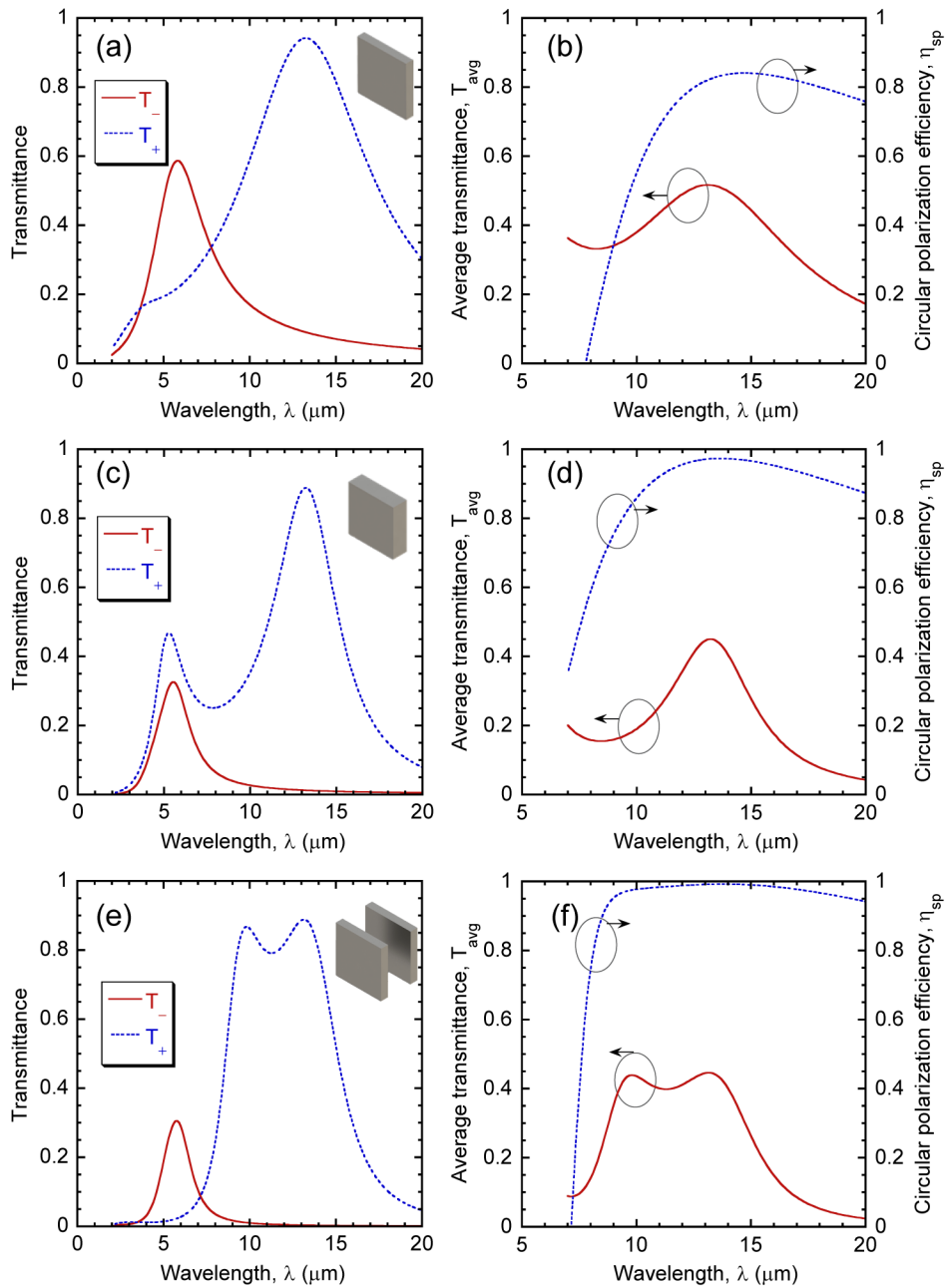
Fig. 2. Transmittance for both LCP and RCP, average transmittance, and circular polarization efficiency for three different structures at normal incidence. (a,b) Single layer with thickness $t = 0.3\,\mu m$; (c,d) single layer with $t = 0.6\,\mu m$; (e,f) two layers separated by $d = 1\,\mu m$ with the same thickness $t = 0.3\,\mu m$. Note that (a,c,e) are for transmittance of individual polarization and (b,d,f) are for the average transmittance and polarization efficiency.

WSM behaves as a metal for LCP and a dielectric for RCP. The transmittance and reflectance components for linear polarization are shown in Figs. 3(c) and 3(d), respectively. The transmittance and reflectance components for linear polarization are independent of the polarization state

at normal incidence. For co-polarization, $R_{pp} = R_{ss}$ and $T_{pp} = T_{ss}$; and for cross-polarization, $R_{ps} = R_{sp}$ and $T_{ps} = T_{sp}$, which are nonzero. Although the Fresnel coefficients have the same absolute value when interchanging their indexes (i.e., $|r_{ps}| = |r_{sp}|$ and $|t_{ps}| = |t_{sp}|$), a π-phase shift exists for cross-polarization transmission coefficient and co-polarization reflection coefficient (i.e., $r_{pp} = -r_{ss}$, $t_{ps} = -t_{sp}$), while the other coefficients have the same sign (i.e., $r_{ps} = r_{sp}$, $t_{pp} = t_{ss}$). This leads to the co-polarization reflectance and cross-polarization reflectance to be zero for circular polarization according to Eq. (6).
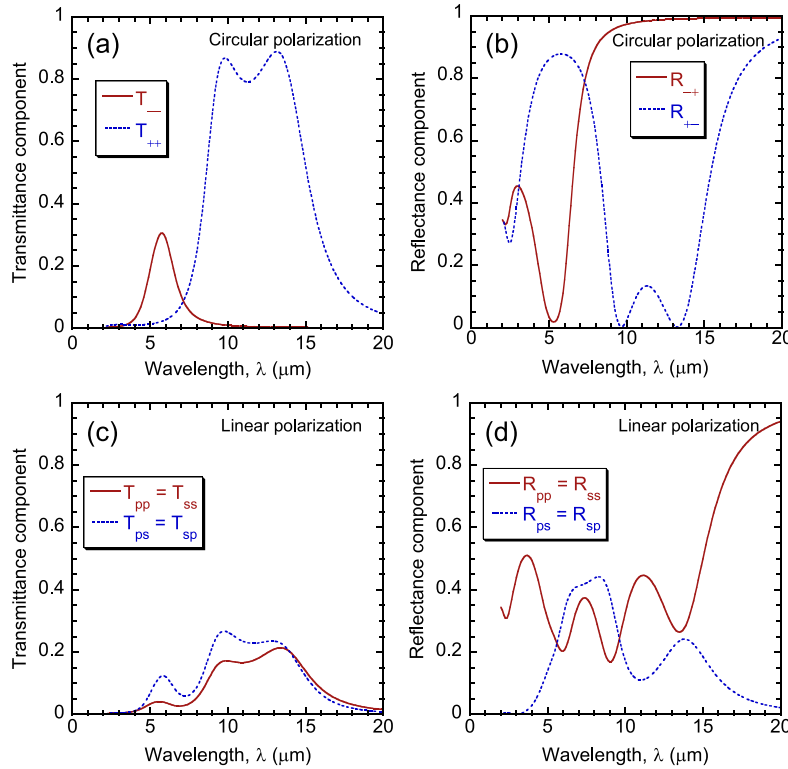
Fig. 3. Transmittance and reflectance components for circular and linear polarizations of the proposed double-WSM-layer structure. (a) Transmittance components for circular polarization. Note that $T_{-+} = T_{+-} = 0$ and not plotted; (b) Reflectance components for circular polarization. Similarly, $R_{--} = R_{++} = 0$ and are not plotted; (c) Transmittance components for linear polarization; and (d) reflectance components for linear polarization.

For the double-WSM-layer polarizer, high average transmittance with high circular polarization efficiency is not limited to normal incidence. The contours of the circular polarization efficiency η_{cp} and average transmittance T_{avg} are plotted in Figs. 4(a) and 4(b), respectively for 7 μm < λ < 20 μm and $0° < \theta_i < 90°$. The parameters are the same as for Figs. 2(e) and 2(f). The plane of incidence defined is the *x-z* plane though rotating the plane of incidence about the *z*-axis does not affect the results. As shown in Fig. 4(a), η_{cp} is greater than ≈ 0.75 at $\theta_i = 50°$ and greater than ≈ 0.92 at $\theta_i = 30°$ for 8 μm < λ < 20 μm. The average transmittance T_{avg}, as shown in Fig. 4(b), is relatively high for 9 μm < λ < 14 μm, and the high transmission band is insensitive to the incidence angle for $\theta_i < 70°$. Clearly, the proposed WSM polarizer possesses a considerable bandwidth with a wide acceptance angle. For example, $\eta_{cp} > 0.8$ and $T_{avg} > 0.3$ can be achieved concurrently at wavelengths from 9 μm to 14 μm and angle of incidence of $0° < \theta_i < 53°$. For oblique incidence with $\theta_i = 50°$, the transmittance components

of circular and linear polarization are plotted in Fig. 4(c) and Fig. 4(d), respectively. Due to oblique incidence, the circular cross-polarization components T_{-+} and T_{+-} are no longer zero and the linear co-polarization components T_{pp} and T_{ss} are not equal to each other. The circular polarization efficiency consequently decreases as cross-polarization components increases.
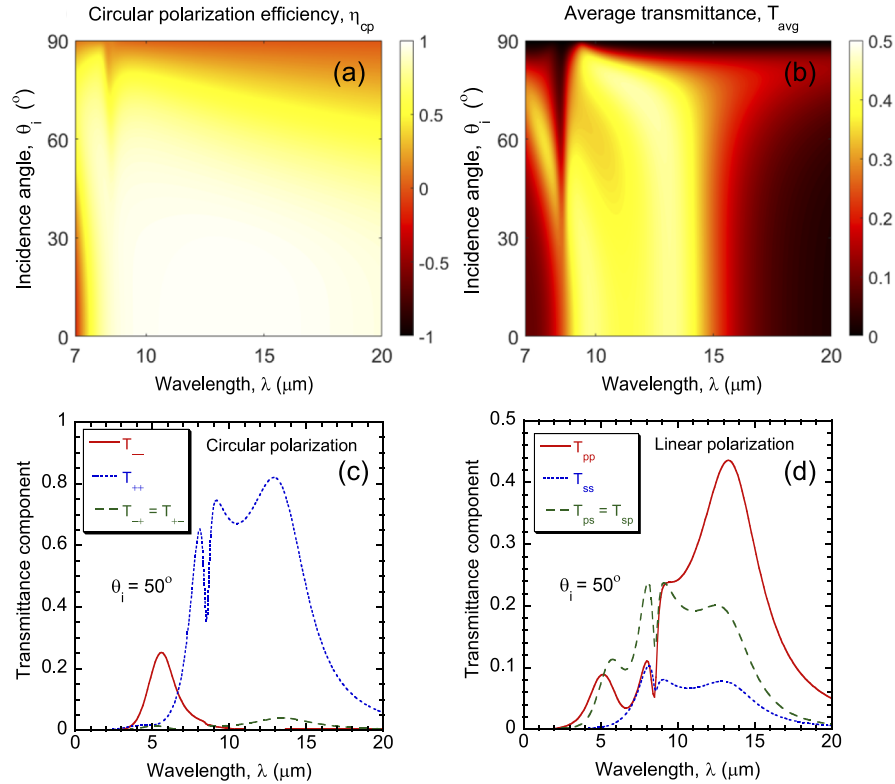
Fig. 4. The effect of oblique incidence on the performance of circular polarizer. Contour plots of (a) circular polarization efficiency and (b) average transmittance as a function of incidence angle and wavelength from $7\,\mu m$ to $20\,\mu m$. At $\theta_i = 50°$, the transmittance components of (c) circular polarization, and (d) linear polarization are plotted.

In practical operation, the polarizer may be subject to different temperature environments. Zhao et al. [32] noted that the application based on WSMs may be highly temperature-sensitive, such as the nonreciprocal thermal emitter. The effect of temperature arises by the dependence of the Fermi energy (also called the chemical potential) E_F that is a function of temperature Θ [44]. Consequently, the bulk conductivity and the diagonal dielectric function will also change. The effects of temperature on the performance are illustrated in Figs. 5(a) and 5(b) by calculating η_{cp} and T_{avg} at three different temperatures $\Theta = 100\,K$, $300\,K$, and $500\,K$. It can be seen that the circular polarization efficiency maintains to be high at wavelengths from $10\,\mu m$ to $20\,\mu m$, while the transmittance band shifts toward longer wavelengths as the temperature increases. Furthermore, the average transmittance at $100\,K$ is higher than that at room temperature; however, there is a reduction in T_{avg} at elevate temperatures, presumably due to loss or absorption that increases with temperature. While lower temperature operation is preferred, due to the high circular polarization efficiency, a moderate temperature increase would not significantly deteriorate the polarizer performance.
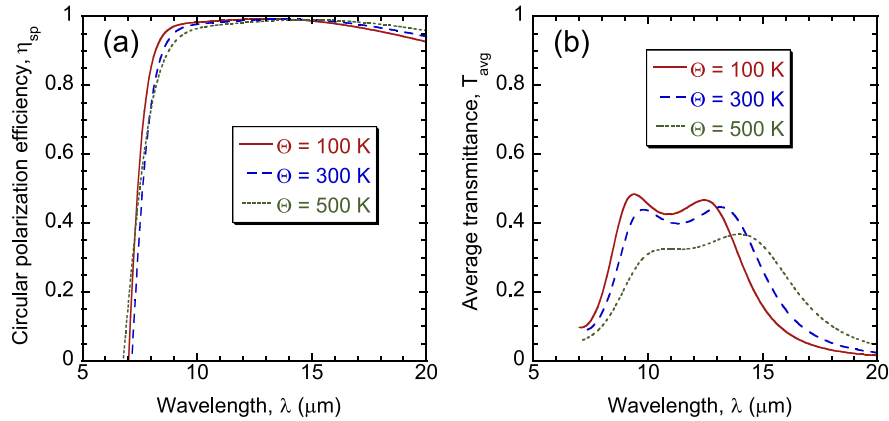
Fig. 5. Temperature dependence of the circular polarizer at normal incidence. (a) Circular polarization efficiency and (b) average transmittance at three different temperatures $\Theta = 100$ K, 300 K, and 500 K.

4. Conclusion

In summary, a high-transmittance mid-infrared circular polarizer is theoretically demonstrated with a simple structure based on magnetic Weyl semimetals. The proposed double-WSM-layer polarizer possesses high circular polarization efficiency that is insensitive to the incidence angle. Tuning the distance of the gap between the two WSM films allows the transmission spectra to be modified to achieve high circular polarization efficiency and high transmittance simultaneously in the wavelength from 9 μm to 15 μm. The circular polarization selectivity can be varied by flipping the polarizer or the direction of Weyl nodes separation vector **b**. Furthermore, the performance of the polarizer can be maintained in a large temperature range, allowing it to operate in versatile conditions. This work provides the technological prospect of a WSM polarizer that is promising for application in infrared spectroscopy and polarimetry.

Appendix A: Derivation of the modified constitutive relation

According to axion electrodynamics [56], an additional term needs to be added to the electro-magnetic Lagrangian density [19,32]:

$$\mathcal{L}_\theta = 2\alpha \sqrt{\frac{\varepsilon_0}{\mu_0}} \frac{\theta(\mathbf{r}, t)}{2\pi} \mathbf{E} \cdot \mathbf{B} \tag{8}$$

where μ_0 is the vacuum permeability, $\alpha = e^2 / (4\pi\varepsilon_0\hbar c)$ is the fine structure constant with $c = 1/\sqrt{\varepsilon_0\mu_0}$ being the speed of light in vacuum, and $\theta(\mathbf{r},t) = 2(\mathbf{b}\cdot\mathbf{r} - b_0 t)$ is the axion angle with b_0 being the separation of Weyl nodes in energy space. Since the two Weyl nodes of interest have the same chemical potential, b_0 is set to be zero. The additional term will change the charge density and current response [56,57], the modified Maxwell's curl equations are expressed as

$$\nabla \times \mathbf{E} = -\frac{\partial \mathbf{B}}{\partial t} \tag{9}$$

$$\nabla \times \mathbf{H} = \frac{\partial(\varepsilon_0\varepsilon_b\mathbf{E})}{\partial t} + \mathbf{J} + \frac{2\alpha}{\pi}\sqrt{\frac{\varepsilon_0}{\mu_0}} \mathbf{b} \times \mathbf{E} \tag{10}$$

where **H** is the magnetic field ($\mathbf{B} = \mu\mu_0\mathbf{E}$), **J** is the ordinary (nonaxion) current, and ε_b is the background relative permittivity (assuming that the material is isotropic in the absence of the

current terms). Combining Eqs. (9) and (10) yields

$$\nabla \times \nabla \times \mathbf{E} = \mu \frac{\omega^2}{c^2} \left(\varepsilon_{\mathrm{b}} \mathbf{E} + \frac{i\sigma}{\omega\varepsilon_0} \mathbf{E} + i\frac{2\alpha c}{\omega\pi} \mathbf{b} \times \mathbf{E} \right). \tag{11}$$

An effective displacement field can be defined as

$$\nabla \times \mathbf{H} = \frac{\partial \mathbf{D}}{\partial t} = \varepsilon_0 \frac{\partial(\bar{\bar{\varepsilon}} \mathbf{E})}{\partial t} \tag{12}$$

so that $\nabla \times \nabla \times \mathbf{E} = \mu\frac{\omega^2}{c^2}(\bar{\bar{\varepsilon}} \mathbf{E})$. Therefore,

$$\mathbf{D} = \varepsilon_0 \bar{\bar{\varepsilon}} \mathbf{E} = \varepsilon_0 \left(\varepsilon_{\mathrm{b}} + \frac{i\sigma}{\omega\varepsilon_0} \right) \mathbf{E} + \frac{ie^2}{2\pi^2\hbar\omega} \mathbf{b} \times \mathbf{E} \tag{13}$$

which is identical to Eq. (1), after the substitution of ε_{d} from Eq. (4).

Disclosures. The authors declare no conflicts of interest.

Data availability. Data of the results presented in this paper are available upon reasonable request from the authors.

References

1. M. Faraday, "I. Experimental researches in electricity.—Nineteenth series," Philos. Trans. R. Soc. London **136**, 1–20 (1846).
2. M. Decker, M. W. Klein, M. Wegener, and S. Linden, "Circular dichroism of planar chiral magnetic metamaterials," Opt. Lett. **32**(7), 856 (2007).
3. Z. Wang, H. Jia, K. Yao, W. Cai, H. Chen, and Y. Liu, "Circular dichroism metamirrors with near-perfect extinction," ACS Photonics **3**(11), 2096–2101 (2016).
4. X. Wu, C. Fu, and Z. M. Zhang, "Chiral response of a twisted bilayer of hexagonal boron nitride," Opt. Commun. **452**, 124–129 (2019).
5. O. Hosten and P. Kwiat, "Observation of the spin Hall effect of light via weak measurements," Science **319**(5864), 787–790 (2008).
6. G. Cao, H.-X. Xu, L.-M. Zhou, Y. Deng, Y. Zeng, S. Dong, Q. Zhang, Y. Li, H. Yang, Q. Song, X. Liu, Y. Li, and C.-W. Qiu, "Infrared metasurface-enabled compact polarization nanodevices," Mater. Today **50**, 499 (2021)..
7. Z. M. Zhang, *Nano/Microscale Heat Transfer*, 2nd ed. (Springer, 2020).
8. F. Snik, J. Craven-Jones, M. Escuti, S. Fineschi, D. Harrington, A. De Martino, D. Mawet, J. Riedi, and J. S. Tyo, "An overview of polarimetric sensing techniques and technology with applications to different research fields," Proc. SPIE **9099**, 90990B (2014).
9. D. H. Goldstein, *Polarized Light*, 3rd ed. (CRC press, 2011).
10. Y. Huang, Y. Zhou, and S.-T. Wu, "Broadband circular polarizer using stacked chiral polymer films," Opt. Express **15**(10), 6414–6419 (2007).
11. W. Cai and V. M. Shalaev, *Optical Metamaterials* (Springer, 2010).
12. J. K. Gansel, M. Thiel, M. S. Rill, M. Decker, K. Bade, V. Saile, G. Von Freymann, S. Linden, and M. Wegener, "Gold helix photonic metamaterial as broadband circular polarizer," Science **325**(5947), 1513–1515 (2009).
13. J. Kaschke, J. K. Gansel, and M. Wegener, "On metamaterial circular polarizers based on metal N-helices," Opt. Express **20**(23), 26012–26020 (2012).
14. Y. Zhao, M. A. Belkin, and A. Alù, "Twisted optical metamaterials for planarized ultrathin broadband circular polarizers," Nat. Commun. **3**(1), 870 (2012).
15. Z. Li, W. Liu, H. Cheng, S. Chen, and J. Tian, "Spin-selective transmission and devisable chirality in two-layer metasurfaces," Sci. Rep. **7**(1), 8204 (2017).
16. S.-E. Mun, J. Hong, J.-G. Yun, and B. Lee, "Broadband circular polarizer for randomly polarized light in few-layer metasurface," Sci. Rep. **9**(1), 2543 (2019).
17. B. Yan and C. Felser, "Topological materials: Weyl semimetals," Annu. Rev. Condens. Matter Phys. **8**(1), 337–354 (2017).
18. P. Hosur and X. Qi, "Recent developments in transport phenomena in Weyl semimetals," C. R. Phys. **14**(9-10), 857–870 (2013).

19. A. A. Zyuzin and A. A. Burkov, "Topological response in Weyl semimetals and the chiral anomaly," Phys. Rev. B **86**(11), 115133 (2012).

20. M. Z. Hasan and C. L. Kane, "Colloquium: topological insulators," Rev. Mod. Phys. **82**(4), 3045–3067 (2010).

21. X.-L. Qi, T. L. Hughes, and S.-C. Zhang, "Topological field theory of time-reversal invariant insulators," Phys. Rev. B **78**(19), 195424 (2008).

22. M. Shuichi, "Phase transition between the quantum spin Hall and insulator phases in 3D: emergence of a topological gapless phase," New J. Phys. **9**(9), 356 (2007).

23. B. Q. Lv, H. M. Weng, B. B. Fu, X. P. Wang, H. Miao, J. Ma, P. Richard, X. C. Huang, L. X. Zhao, G. F. Chen, Z. Fang, X. Dai, T. Qian, and H. Ding, "Experimental discovery of Weyl semimetal TaAs," Phys. Rev. X **5**, 031013 (2015).

24. S. Y. Xu, I. Belopolski, N. Alidoust, M. Neupane, G. Bian, C. Zhang, R. Sankar, G. Chang, Z. Yuan, C. C. Lee, S. M. Huang, H. Zheng, J. Ma, D. S. Sanchez, B. Wang, A. Bansil, F. Chou, P. P. Shibayev, H. Lin, S. Jia, and M. Z. Hasan, "Discovery of a Weyl fermion semimetal and topological Fermi arcs," Science **349**(6248), 613–617 (2015).

25. D. F. Liu, A. J. Liang, E. K. Liu, Q. N. Xu, Y. W. Li, C. Chen, D. Pei, W. J. Shi, S. K. Mo, P. Dudin, T. Kim, C. Cacho, G. Li, Y. Sun, L. X. Yang, Z. K. Liu, S. S. P. Parkin, C. Felser, and Y. L. Chen, "Magnetic Weyl semimetal phase in a Kagomé crystal," Science **365**(6459), 1282–1285 (2019).

26. K. Kuroda, T. Tomita, M. T. Suzuki, C. Bareille, A. P. Goswami, M. Ochi, M. Ikhlas, M. Nakayama, S. Akebi, R. Noguchi, R. Ishii, N. Inami, K. Ono, H. Kumigashira, A. Varykhalov, T. Muro, T. Koretsune, R. Arita, S. Shin, T. Kondo, and S. Nakatsuji, "Evidence for magnetic Weyl fermions in a correlated metal," Nat. Mater. **16**(11), 1090–1095 (2017).

27. A. B. Sushkov, J. B. Hofmann, G. S. Jenkins, J. Ishikawa, S. Nakatsuji, S. Das Sarma, and H. D. Drew, "Optical evidence for a Weyl semimetal state in pyrochlore Eu$_2$Ir$_2$O$_7$," Phys. Rev. B **92**(24), 241108 (2015).

28. G. Xu, H. Weng, Z. Wang, X. Dai, and Z. Fang, "Chern semimetal and the quantized anomalous Hall effect in HgCr$_2$Se$_4$," Phys. Rev. Lett. **107**(18), 186806 (2011).

29. J. Kübler and C. Felser, "Weyl points in the ferromagnetic Heusler compound Co$_2$MnAl," EPL **114**(4), 47005 (2016).

30. Y. Okamura, S. Minami, Y. Kato, Y. Fujishiro, Y. Kaneko, J. Ikeda, J. Muramoto, R. Kaneko, K. Ueda, V. Kocsis, N. Kanazawa, Y. Taguchi, T. Koretsune, K. Fujiwara, A. Tsukazaki, R. Arita, Y. Tokura, and Y. Takahashi, "Giant magneto-optical responses in magnetic Weyl semimetal Co$_3$Sn$_2$S$_2$," Nat. Commun. **11**(1), 4619 (2020).

31. V. S. Asadchy, C. Guo, B. Zhao, and S. Fan, "Sub-wavelength passive optical isolators using photonic structures based on Weyl semimetals," Adv. Opt. Mater. **8**(16), 2000100 (2020).

32. B. Zhao, C. Guo, C. A. C. Garcia, P. Narang, and S. Fan, "Axion-field-enabled nonreciprocal thermal radiation in Weyl semimetals," Nano Lett. **20**(3), 1923–1927 (2020).

33. Y. Tsurimaki, X. Qian, S. Pajovic, F. Han, M. Li, and G. Chen, "Large nonreciprocal absorption and emission of radiation in type-I Weyl semimetals with time reversal symmetry breaking," Phys. Rev. B **101**(16), 165426 (2020).

34. Y. Gao and J. Qi, "Chiral terahertz emission from the Weyl semimetals," in *2020 IEEE Asia-Pacific Microwave Conference (APMC)*, (2020), 475–476.

35. Y. Wang, C. Khandekar, X. Gao, T. Li, D. Jiao, and Z. Jacob, "Broadband circularly polarized thermal radiation from magnetic Weyl semimetals," Opt. Mater. Express **11**(11), 3880–3895 (2021).

36. P. Hosur and X.-L. Qi, "Tunable circular dichroism due to the chiral anomaly in Weyl semimetals," Phys. Rev. B **91**(8), 081106 (2015).

37. J. R. Soh, F. De Juan, M. G. Vergniory, N. B. M. Schröter, M. C. Rahn, D. Y. Yan, J. Jiang, M. Bristow, P. A. Reiss, J. N. Blandy, Y. F. Guo, Y. G. Shi, T. K. Kim, A. McCollam, S. H. Simon, Y. Chen, A. I. Coldea, and A. T. Boothroyd, "Ideal Weyl semimetal induced by magnetic exchange," Phys. Rev. B **100**(20), 201102 (2019).

38. J. Hofmann and S. Das Sarma, "Surface plasmon polaritons in topological Weyl semimetals," Phys. Rev. B **93**(24), 241402 (2016).

39. V. S. Asadchy, M. S. Mirmoosa, A. Diaz-Rubio, S. Fan, and S. A. Tretyakov, "Tutorial on electromagnetic nonreciprocity and its origins," Proc. IEEE **108**(10), 1684–1727 (2020).

40. Z. M. Zhang, X. Wu, and C. Fu, "Validity of Kirchhoff's law for semitransparent films made of anisotropic materials," J. Quant. Spectrosc. Radiat. Transf. **245**, 106904 (2020).

41. O. V. Kotov and Y. E. Lozovik, "Giant tunable nonreciprocity of light in Weyl semimetals," Phys. Rev. B **98**(19), 195446 (2018).

42. O. V. Kotov and Y. E. Lozovik, "Dielectric response and novel electromagnetic modes in three-dimensional Dirac semimetal films," Phys. Rev. B **93**(23), 235417 (2016).

43. P. S. Pershan, "Magneto-Optical Effects," J. Appl. Phys. **38**(3), 1482–1490 (1967).

44. P. E. C. Ashby and J. P. Carbotte, "Chiral anomaly and optical absorption in Weyl semimetals," Phys. Rev. B **89**(24), 245121 (2014).

45. X. Liu, S. Fang, Y. Fu, W. Ge, M. Kareev, J.-W. Kim, Y. Choi, E. Karapetrova, Q. Zhang, L. Gu, E.-S. Choi, F. Wen Justin, and G. Fabbris, Philip, J. Freeland, D. Haskel, W. Wu Jedediah and J. Chakhalian, "A magnetic Weyl semimetallic phase in thin films of Eu2Ir2O7," arXiv:2106.04062v1 (2021).

46. S. Li, G. Gu, E. Liu, P. Cheng, B. Feng, Y. Li, L. Chen, and K. Wu, "Epitaxial growth and transport properties of magnetic Weyl semimetal Co$_3$Sn$_2$S$_2$ thin films," ACS Appl. Electron. Mater. **2**(1), 126–133 (2020).

47. A. K. Zvezdin and V. A. Kotov, *Modern Magnetooptics and Magnetooptical Materials* (CRC Press, 1997).

48. S. Teitler and B. W. Henvis, "Refraction in Stratified, Anisotropic Media*," J. Opt. Soc. Am. **60**(6), 830–834 (1970).

49. D. W. Berreman, "Optics in stratified and anisotropic media: 4×4-matrix formulation," J. Opt. Soc. Am. **62**(4), 502–510 (1972).
50. G. D. Landry and T. A. Maldonado, "Complete method to determine transmission and reflection characteristics at a planar interface between arbitrarily oriented biaxial media," J. Opt. Soc. Am. A **12**(9), 2048–2063 (1995).
51. M. Schubert, "Polarization-dependent optical parameters of arbitrarily anisotropic homogeneous layered systems," Phys. Rev. B **53**(8), 4265–4274 (1996).
52. X. Wu, C. Fu, and Z. M. Zhang, "Effect of orientation on the directional and hemispherical emissivity of hyperbolic metamaterials," Int. J. Heat Mass Transf. **135**, 1207–1217 (2019).
53. C. Menzel, C. Rockstuhl, and F. Lederer, "Advanced Jones calculus for the classification of periodic metamaterials," Phys. Rev. A **82**(5), 053811 (2010).
54. C. Khandekar, F. Khosravi, Z. Li, and Z. Jacob, "New spin-resolved thermal radiation laws for nonreciprocal bianisotropic media," New J. Phys. **22**(12), 123005 (2020).
55. M. Bass, *Handbook of Optics, Volume I: Geometrical and Physical Optics, Polarized Light, Components and Instruments*, 3rd ed. (McGraw-Hill, 2010).
56. F. Wilczek, "Two applications of axion electrodynamics," Phys. Rev. Lett. **58**(18), 1799–1802 (1987).
57. M. Kargarian, M. Randeria, and N. Trivedi, "Theory of Kerr and Faraday rotations and linear dichroism in Topological Weyl Semimetals," Sci. Rep. **5**(1), 12683 (2015).